Probing electrolyte influence on CO_2 reduction in aprotic solvents

Reginaldo J. Gomes†, Chris Birch†, Morgan M. Cencer‡, Chenyang Li‡, Seoung-Bum Son§, Ira D. Bloom§, Rajeev S. Assary‡, and ‡ Chibueze V. Amanchukwu†§*

†Pritzker School of Molecular Engineering, The University of Chicago, Chicago, IL, 60637

‡Materials Science Division, Argonne National Laboratory, Lemont, IL, 60439

§Chemical Sciences and Engineering Division, Argonne National Laboratory, Lemont, IL, 60439

*Corresponding author

Email: chibueze@uchicago.edu

Abstract

Selective CO_2 capture and electrochemical conversion is an important tool in the fight against climate change. Industrially, CO_2 is captured using a variety of aprotic solvents due to their high CO_2 solubility. However, most research efforts on electrochemical CO_2 conversion use aqueous media and are plagued by competing hydrogen evolution reaction (HER) from water breakdown. Fortunately, aprotic solvents can circumvent HER; making it important to develop strategies that enable integrated CO_2 capture and conversion in an aprotic solvent. However, the influence of ion solvation and solvent selection within nonaqueous electrolytes for efficient and selective CO_2 reduction is unclear. In this work, we show that bulk solvation behavior within the nonaqueous electrolyte can control the CO_2 reduction reaction and product distribution occurring at the catalyst-electrolyte interface. We study different TBA (tetrabutylammonium) salts in two electrolyte systems with glyme-ethers (e.g., 1,2 dimethoxyethane or DME) and dimethylsulfoxide (DMSO) as a low and high dielectric constant medium, respectively. Using spectroscopic tools, we quantify the fraction of ion pairs that form within the electrolyte and show how ion-pair formation is prevalent in DME electrolytes and is dependent on anion type. More importantly, we show as ion-pair formation decreases within the electrolyte, CO_2 current densities increases, and a higher CO Faradaic efficiency is observed at low overpotentials. Meanwhile, in an electrolyte medium where ion-pair fraction does not change with anion type (such as in DMSO), a smaller influence of solvation was observed on CO_2 current densities and product distribution. By directly coupling bulk solvation to interfacial reactions and product distribution, we showcase the importance and utility of controlling the reaction microenvironment in tuning electrocatalytic reaction pathways. Insights gained from this work will enable novel electrolyte design for efficient and selective CO_2 conversion to desired fuels and chemicals.

Introduction

Lower renewable electricity costs and continued emission of greenhouse gases have spurred the electrochemical reduction of carbon dioxide (CO_2) as a viable option for fuels and chemical production[1–4]**.** Currently, the most prevalent approach for CO_2 electrochemical reduction reaction (CO_2RR) consists of CO_2 heterogeneous catalysis over a metallic electrode. This approach has yielded a myriad of CO_2RR products, spanning from carbon monoxide to multi carbon/multi hydrogenated products, such as ethylene, ethanol, and n-butanol [5–7]. However, CO_2RR in an aqueous medium is always plagued by the competing hydrogen evolution reaction (HER), [8,9] which happens at similar electrochemical potentials. Moreover, CO_2 mass transport is often limited by poor CO_2 solubility in water and the competing equilibrium between CO_2 and carbonate species at medium to high pH[10,11].

One strategy to circumvent the competing HER is to use solvents other than water[12]. Organic solvents such as acetonitrile (ACN), dimethylformamide (DMF), and dimethyl sulfoxide (DMSO) can suppress HER because they do not have any easily ionizable protons that could be further reduced. When combined with either organic salts or ionic liquids, these aprotic solvents have enabled faradaic efficiency (FE) values above 90% for carbon monoxide[13,14], formic acid[15,16], and oxalic acid[17]. Moreover, CO_2 mass transport can be facilitated in these solvents due to their high CO_2 solubility when compared to water[15,18,19]. Aprotic solvents have been used industrially for CO_2 physical absorption, such as dimethyl ethers of polyethylene glycol (Selexol™ or Coastal AGR®), N-Methyl-2-pyrrolidone (Purisol®), and propylene carbonate (Fluor Solvent™)[20,21]. Therefore, the use of aprotic solvent for CO_2RR could leverage the development of new technologies that integrate both CO_2 capture and conversion.

In addition to solvent effects, the nature of the supporting electrolyte also plays an important role in the CO_2RR current density and selectivity. For an aqueous medium, it has been widely reported that large alkaline cations (such as Cs^+) can enhance CO_2RR current densities and the formation of multi carbon products by stabilizing high dipole intermediates at the electrode surface through short and medium-range interactions[22–24]. On the other hand, different anions can functionalize the electrode surface and facilitate CO_2 activation by partial charge donation from the anion to the adsorbed CO_2 molecule[25–27]. However, the role of the electrolyte (salt and solvent) in the CO_2RR performance in an aprotic medium is still controversial. Voltammetric studies conducted in DMF with quaternary ammonium salts have shown that the nature of either the cation or the anion has little or no effect on the CO_2RR current density[28,29]. In contrast, experimental studies conducted in ACN with tetraethylammonium salts have concluded that switching the counterion from BF_4^- to triflate (OTf^-) results in a significant increase in current densities, which was only attributed to differences in solution water content[30]. Moreover, the nature of the anionic species

has also played an important role in dictating the product distribution towards either formic acid or HER in ACN/ionic-liquid/water mixtures[16].

Recent studies in the Li-O_2[31,32] and Na-O_2 battery literature[33] have shown that electrolyte solvation can be modulated to control the oxygen reduction reaction (ORR) pathway. Therefore, the differences in CO_2RR electrochemical performance in aprotic solvents might also be dictated by the electrolyte solvation behavior. For example, in Li-O_2 batteries, low donor number solvents such as glyme-ethers lead to a surface-driven ORR pathway due to poor superoxide (O_2^-) solubility, while high donor number solvents such as DMSO with high O_2^- solubility leads to a solution-driven ORR pathway[34]. Differences in electrolyte solvation, and thereby transport and electrochemical properties, are more accentuated when using a low coordinating solvent. For instance, solvation in weakly coordinating glyme-ethers presents a strong dependence of the anion basicity[33] and solvent chain length[35]. In contrast, the nature of the anion presents a weaker effect in electrolyte solvation[33], ion mobility [36], and oxygen activity[37] in the highly coordinating DMSO.

In this work, we investigated the solvation effects on the CO_2RR performance in aprotic solvents. We selected two widely different solvents, 1,2-dimethoxyethane (DME) and DMSO, to further correlate bulk solvation properties to electrochemistry performance. Surprisingly, there are no studies reported on the use of any glyme-ethers in CO_2RR, despite their large electrochemical window, high CO_2 solubility, and industrial relevance for CO_2 capture. We show that the CO_2RR current density correlates with the ether chain length, solvent choice (DMSO versus DME), tetrabutylammonium (TBA) salt concentration, and the salt anion (solvents and salts structures herein investigated are illustrated in Scheme 1). We quantify the influence of salt on the solvation behavior in DME and DMSO-based electrolytes and show that a higher fraction of ion aggregates in DME-based electrolytes lead to lower current densities, where the anion identity controls the propensity for aggregate formation. In contrast, across the TBA salts studied in DMSO, a lower fraction of aggregates was observed, and these anions had little influence on the observed CO_2RR current density. Using Cu as the electrocatalyst, electrolytes with a low population of ion pairs yielded larger FE values for CO at lower overpotentials, while a high population of ion pairs led to high FE values for hydrogen across different potentials. By coupling bulk solvation to interfacial reactions and product distribution, we broadened our understanding of how the electrolyte microenvironment could affect the CO_2RR performance in aprotic systems. Insights gained from this work will facilitate the design of more efficient and selective electrolytes for CO_2 conversion to desired fuels and chemicals.

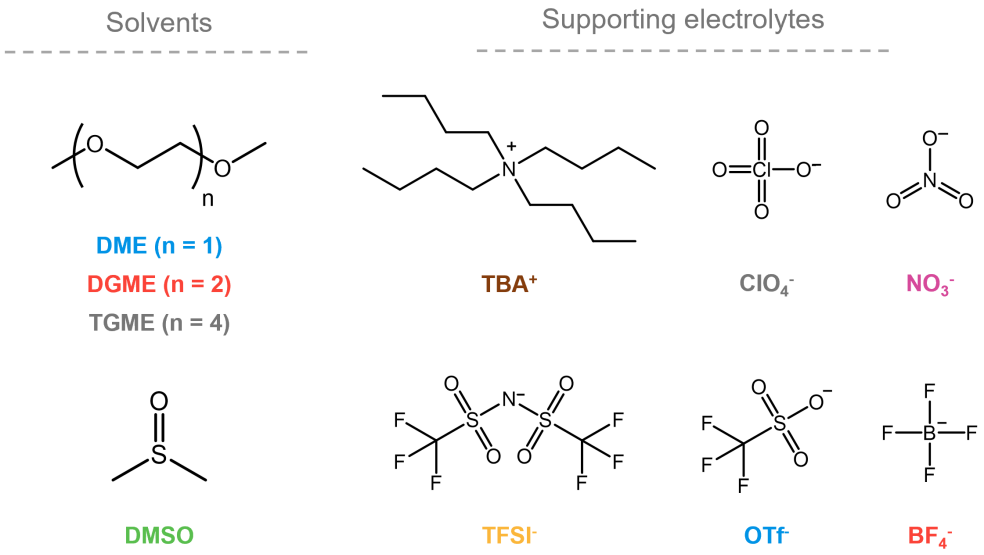

Scheme 1. Chemical structures of the herein investigated solvents and TBA salts. Compounds are 1,2 dimethoxyethane (DME), diglyme (DGME), tetraglyme (TGME), dimethyl sulfoxide (DMSO), tetrabutylammonium (TBA^+), perchlorate (ClO_4^-), nitrate (NO_3^-), bistriflimide ($TFSI^-$), triflate (OTf), tetrafluoroborate (BF_4^-).

Results and discussion

Carbon dioxide reduction in glyme-ethers solvents

Glyme-ethers have been explored for a variety of electrochemical systems, ranging from electrochemical double-layer capacitors[38], to battery chemistries such as lithium metal[39], sodium-ion[40], and non-aqueous redox flow batteries.[41] Their widespread use is attributed to a propensity to dissolve and coordinate alkali cations, high reductive stability, and low viscosities. On the other hand, alkali cations have been the dominant supporting ions within the electrolyte for aqueous CO_2RR since they can enhance the reaction selectivity towards value-added products such as ethylene and ethanol[22–24]. Accessing highly reductive potentials in combination with alkali cations may enable further reduced products. However, in aqueous systems, hydrogen evolution outcompetes CO_2RR at highly reductive potentials where further reduced products may be expected[24,42,43]. Therefore, we hypothesized that combining alkali cations with reductively stable glyme ethers may enable selective CO_2RR.

Linear sweep voltammetry (LSV) was performed to understand the effect of salt selection for CO_2RR in aprotic electrolytes. Figure 1a shows voltammograms of a copper electrode in a DME electrolyte containing dissolved TBA and sodium salts. Potential measurements were standardized to the decamethylferrocenium/decamethylferrocene (Fc*) redox potential, since other authors[28] have indicated that the nature of electrolyte can affect the silver wire reference

electrode potential, thereby leading to false data interpretation. In addition, decamethylferrocene has been reported as more stable compared to ferrocene especially in the presence of radical anions such as superoxide [44,45] and we anticipate similar concerns in the presence of the carbon dioxide radical anion intermediate. Unfortunately, as Figure 1a shows, the presence of sodium ions appears to inhibit CO_2RR at reductive potentials up to -2.8 V (vs. Fc^{*+}/Fc^*); a phenomenon that has been observed by previous authors with different aprotic solvents, such as ACN[30] and DMF[28]. Nevertheless, when $NaClO_4$ salt is replaced by $TBAClO_4$, CO_2RR is observed with an onset potential around -1.8 V. To the best of our knowledge, this is the first report of electrocatalytic CO_2 reduction in a glyme-ether solvent.

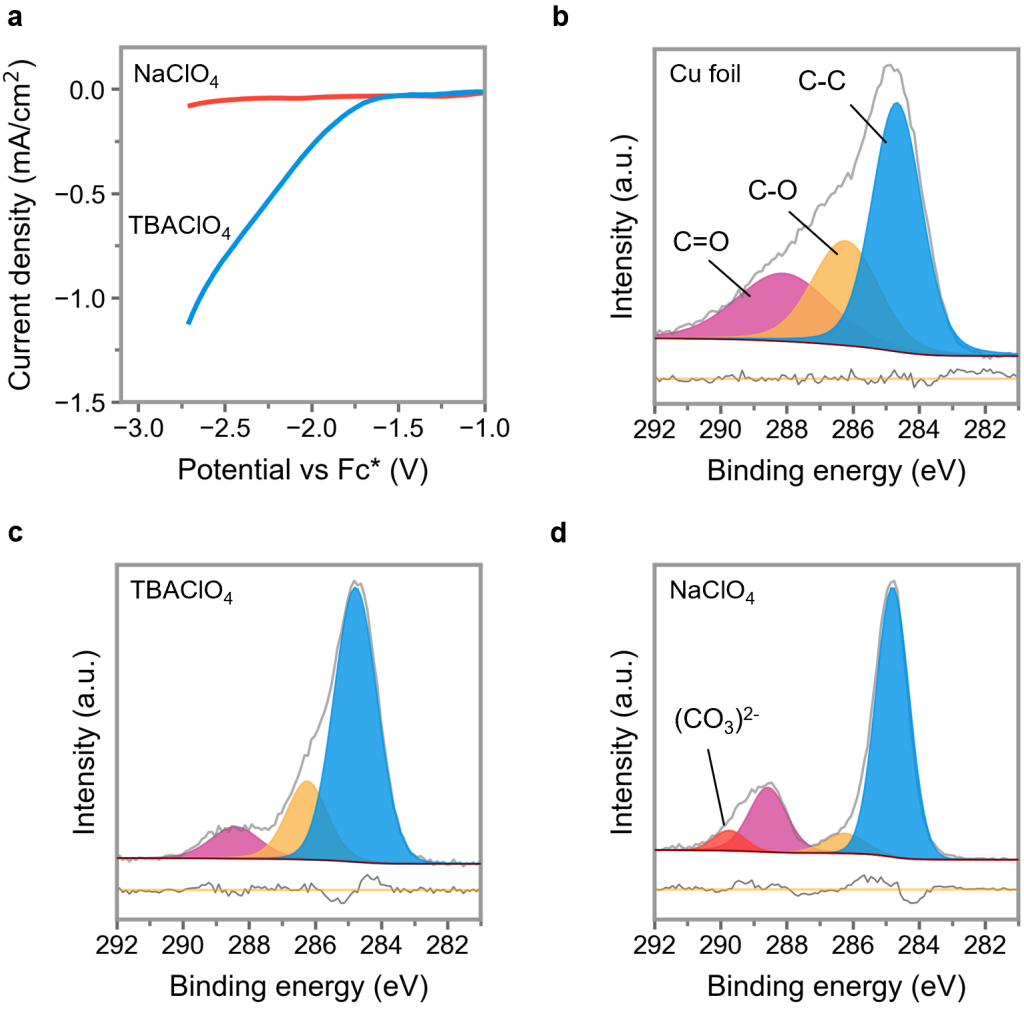

Figure 1. **Influence of cation selection.** (**a**) Linear sweep voltammograms (LSVs) for Cu electrode at 50 mV/s in CO_2 atmosphere in the presence of 0.5 M $NaClO_4$ and 0.5 M $TBAClO_4$ in DME. High-resolution XPS (X-ray photoelectron spectroscopy) C1s spectra of the metallic copper catalyst (**b**) before CO_2RR, after 10 min electrolysis at -2.6 V vs Fc* in DME with electrolytes containing (**c**) $TBAClO_4$, and (**d**) $NaClO_4$ salts.

Previous works[30,46] have suggested that CO_2RR in nonaqueous electrolytes containing alkali cations (M^+) can be deactivated by the competitive reduction of M^+ to M^0. However, the potentials for Na^+ or Li^+ reduction are more negative than the potentials needed for CO_2RR (around -3.0V vs Fc**, see Figure S1). Furthermore, the alkali cation reduction hypothesis is not sufficient to explain the complete inhibition of CO_2RR, since electrodeposition will lead to a reductive current signal[47,48]. To further probe the effect of alkali cation on suppressing CO_2RR, we performed X-ray photoelectron spectroscopy (XPS) on the copper electrode before and after electrolysis in the presence of CO_2. The C1s XPS data in Figures 1b and 1c for pristine Cu foils before and after electrolysis in TBA-containing electrolytes shows no modification of the catalyst surface. However, when an alkali cation is present, a passivation layer of carbonate species is formed on the catalyst surface (Figure 1d). Unlike aqueous electrolytes, these alkali carbonates are insoluble in glyme-ethers, acting as an insulating layer that prevents any further electrochemical reaction on the electrode surface, including the facile Fc^{*+}/Fc^* reversible reference reaction (Figure S2). Similar decay in electrochemical performance has also been observed in metal-CO_2 batteries, where the formation of alkali carbonates in an aprotic medium result in poor rechargeability[49,50]. Hence, TBA salts were chosen to serve as supporting ions to further investigate the influence of the solvent and counter-ion on the CO_2RR performance.

Despite their good reductive stability and high CO_2 solubility, glyme-ethers solvents impose new challenges for the electrochemical reduction of CO_2. As shown in Table 1, all glyme-ethers have low acceptor number (AN), low donor number (DN), and low dielectric constants, which may result in poor salt solubility and low ionic conductivity. Moreover, the increase in the ether chain length results in a significant increase in the dynamic viscosity, which may affect charge mobility and electron transfer rates[51].

Table 1 - Summary of potential glyme-ether solvents and dimethylsulfoxide for CO_2RR, their solvent properties, and CO_2 solubility values.

Solvent		CO_2 solubility (mmol/l)	Permittivity at 25°C	Viscosity [mm^2/s]	DN [$kcal.mol^{-1}$]	AN
1,2-dimethoxyethane	(DME)	227 ± 15*	7.07 [52]	0.5 [53]	20 [54]	10.2 [54]
Diglyme	(DGME)	160 ± 8.3*	7.63 [52]	1.2 [53]	18 [54]	9.9 [54]
Tetraglyme	(TGME)	127 ± 6.3*	7.78 [52]	4.1 [53]	12 [35,55]	10.5 [35,55]
Dimethyl sulfoxide	(DMSO)	130 ± 7 [56]	46.7	2.0[57]	29.8	19.3

*Determined experimentally in this work (further details in the S.I.)

To understand the effect of the solvent properties on the CO_2RR performance, linear sweep voltammetry experiments were first performed at Cu electrodes in 0.5 M TBAOTf in different

glyme-ether solvents (DME, DGME, and TGME). The corresponding voltammograms (LSVs) are presented in Figure 2a. When CO_2 is present, negative reductive currents are observed starting at -1.8V for all 3 glyme-ethers, indicating the CO_2RR onset potential. These similar values in onset potential might indicate that these 3 solvents have similar or no effect on the rate-determining step for CO_2RR, which is usually attributed to the formation of the $CO_2^{\bullet-}$ radical[58,59] especially in aprotic media. On the other hand, an increase in the alkoxy chain length (moving from DME to TGME) resulted in a decrease in the CO_2RR current density. This result can be correlated to a decrease in solution conductivity (Figure 2b), thus indicating that the solvent viscosity may also play a role in dictating the overall CO_2RR performance.

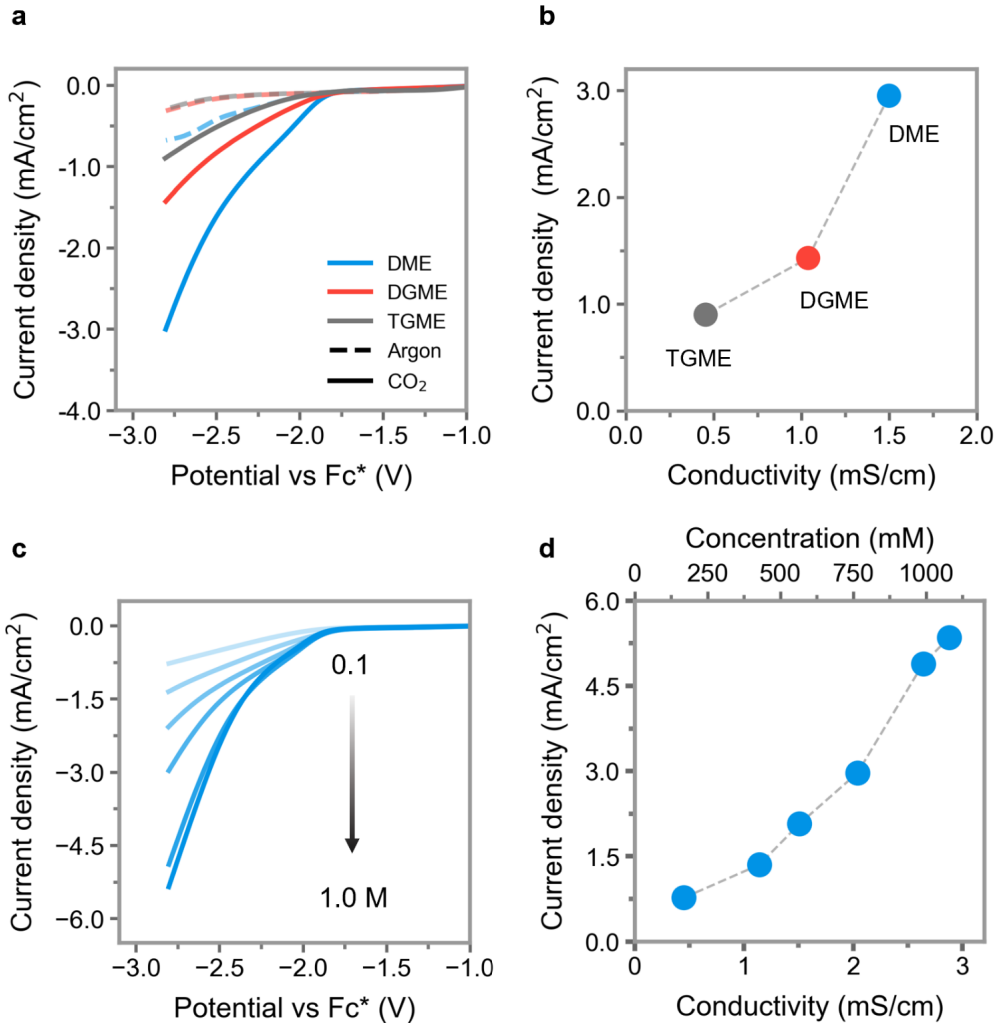

Figure 2. **Influence of glyme-ethers**. (**a**) LSVs for Cu electrode at 50 mV/s in an Argon atmosphere (dashed line) and CO_2 atmosphere (solid lines) in 0.5 M TBAOTf in different glyme-ethers, (**b**) Ionic conductivity of different glyme-ethers solutions containing 0.5M TBAOTf *vs* current density extracted from the respective voltammograms (in **a**) at -2.8V vs Fc*. (**c**) LSVs for Cu electrode at 50 mV/s in CO_2 atmosphere at different salt concentrations (0.1, 0.2, 0.3, 0.5, 0.75, and 1.0M) of TBAOTf in DME, and (**d**) conductivity of solutions containing different

TBAOTf concentrations in DME *vs* current density extracted from the respective voltammograms (in **c**) at -2.8V vs Fc*.

To understand the interplay between solution conductivity and CO_2RR current density, we performed experiments at different salt concentrations. As shown in Figure 2c, the increase in salt concentration up to 750 mM results in a significant increase in the CO_2RR current density in DME. The increase in salt concentration also leads to an increase in solution conductivity (Figure 2d). However, above 750 mM, the increase in current density with salt concentration is less pronounced, most likely because the solution becomes visually more viscous. Therefore, we developed our subsequent studies of CO_2RR in DME at a salt concentration of 500 mM.

Electrolyte effects on CO_2RR current densities

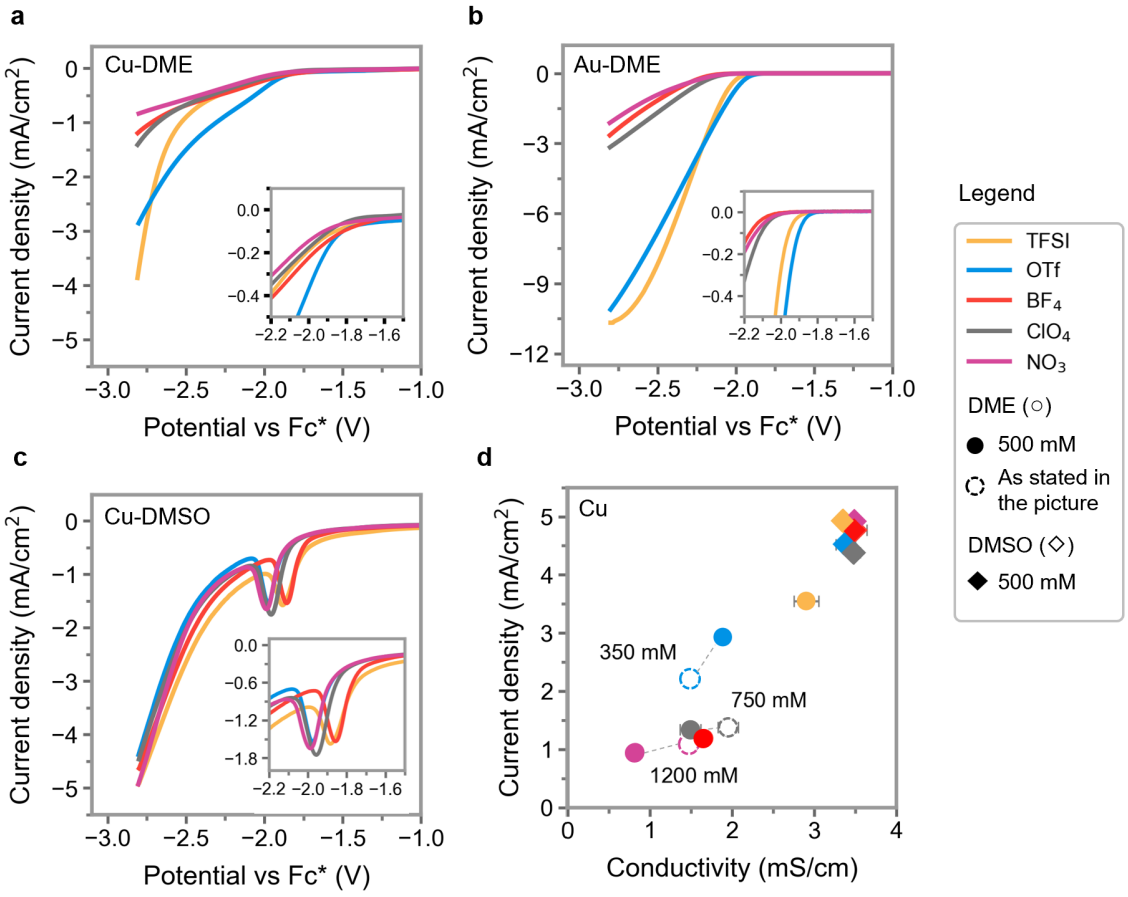

Figure 3. **Catalyst and electrolyte effects**. LSVs in CO_2 atmosphere in the presence of 0.5 M TBA salts at 50 mV/s for (**a**) Cu electrodes in DME, (**b**) Au electrodes in DME, and (**c**) Cu electrodes in DMSO. (**d**) current density extracted from the LSVs plots at -2.8V vs Fc* for Cu electrodes vs solution conductivity at different TBA salt concentrations in both DME and DMSO.

It has been widely reported that the solvation structure of different cationic species in an aqueous medium can directly affect the CO_2RR current density and product distribution[60–62]. However, these studies did not consider the competing formation of ion pairs, which are more commonly observed in non-aqueous solvents due to their poorer ability to solvate ionic species compared to water[36]. In general, the equilibrium between ionic species in solution can be written as $C_{(Sol)} + A_{(Sol)} \rightleftharpoons (C\text{-}A)_{(Sol)}$, where C and A represent the cation and anion respectively, and Sol represents the solvated state. The quaternary ammonium cations used in this work are usually poorly solvated due to the steric hindrance generated by the alkyl groups. Moreover, glyme-ethers weakly coordinate with anionic species due to their low dielectric constant and low AN (acceptor number) values [33], as shown in Table 1. Therefore, the combined characteristics of glyme-ethers and TBA salts can significantly shift the ionic equilibrium to the right, thereby enhancing the role of the anion on the formation of ion pairs.

Figure 3 shows LSVs and conductivity values for 5 different TBA salts. TBA salts containing halides (I^-, Cl^-, and F^-), PF_6^-, and acetate were poorly soluble in DME. As Figure 3a shows, all TBA salts present similar onset values around -1.8 V *vs* Fc* at the Cu electrode in DME. However, the anion nature had a significant effect on the CO_2RR current density. Electrolytes containing OTf^- and $TFSI^-$ can reach current density values around 3 mA/cm^2 and beyond. However, electrolytes containing BF_4^-, ClO_4^-, and NO_3^- presented values below 1.5 mA/cm^2. Unlike previous work[30], we could not ascribe those differences in current density to differences in the electrolyte water content, because it was kept below 100 ppm for all TBA solutions over the LSVs experiments (see Table S1).

To decouple the differences observed in the electrochemical behavior of the TBA salts from any catalyst modification, we further investigated the copper electrode surface after CO_2RR using XPS. Our XPS results (Figure S3) show no major differences for C1s, Cu2p, and O1s for most electrolytes when compared to the pristine copper foil. However, for the electrolyte containing OTf anions, a salt breakdown is observed as a small peak assigned to C-F bonds can be observed in the C1s and F1s spectra. Despite the OTf^- singular behavior, the overall trend in current density observed for different anions was further supported by experiments conducted using a gold electrode. As depicted in Figure 3b, OTf^- and $TFSI^-$ salts again presented higher current density values and onset potential of 0.2V less negative than ClO_4^-, BF_4^-, and NO_3^- salts. As a noble metal, gold electrodes are more stable than copper in the applied potential range in both aqueous and nonaqueous medium[63]. Therefore, the influence of the anion appears the same across different catalysts (Cu and Au) and may not be attributed only to catalyst surface changes.

In contrast to observations in DME, experiments conducted in highly coordinating DMSO (Figure 3c) did not show any significant differences either in current density or onset potential across the

different TBA salts. All DMSO electrolytes presented current density values significantly greater than those observed by the respective salts in DME. Despite the higher current density values observed for all TBA salts in DMSO and OTf^-/$TFSI^-$ salts in DME, it is important to highlight that those electrolytes also presented higher conductivity values when compared to the remaining ClO_4^-, BF_4^-, and NO_3^- salts. As discussed earlier, the solution conductivity in TBAOTf solutions can be directly correlated to the final product current density. To decouple the solution conductivity from the anion effect on the CO_2RR current density, we performed LSVs experiments with solutions containing different salt concentrations in DME. As shown in Figure 3d, electrolytes containing 1200 mM NO_3^-, 500 mM ClO_4^-, and 350 mM OTf present similar conductivity values at around 1.5 mS/cm. However, they still present significant differences in current density, maintaining the previously observed trend where $OTf^- > ClO_4^- > NO_3^-$. We also observed a similar behavior for solutions containing 750 mM ClO_4^- and 500 mM OTf that have similar ionic conductivities (2 mS/cm), but the OTf^- solutions led to higher current densities values. Since the anion effect in DME could not be ascribed to modifications on either electrode surface or solution conductivity, we conducted a more detailed analysis of the electrolyte structure in solution.

Ion solvation studies

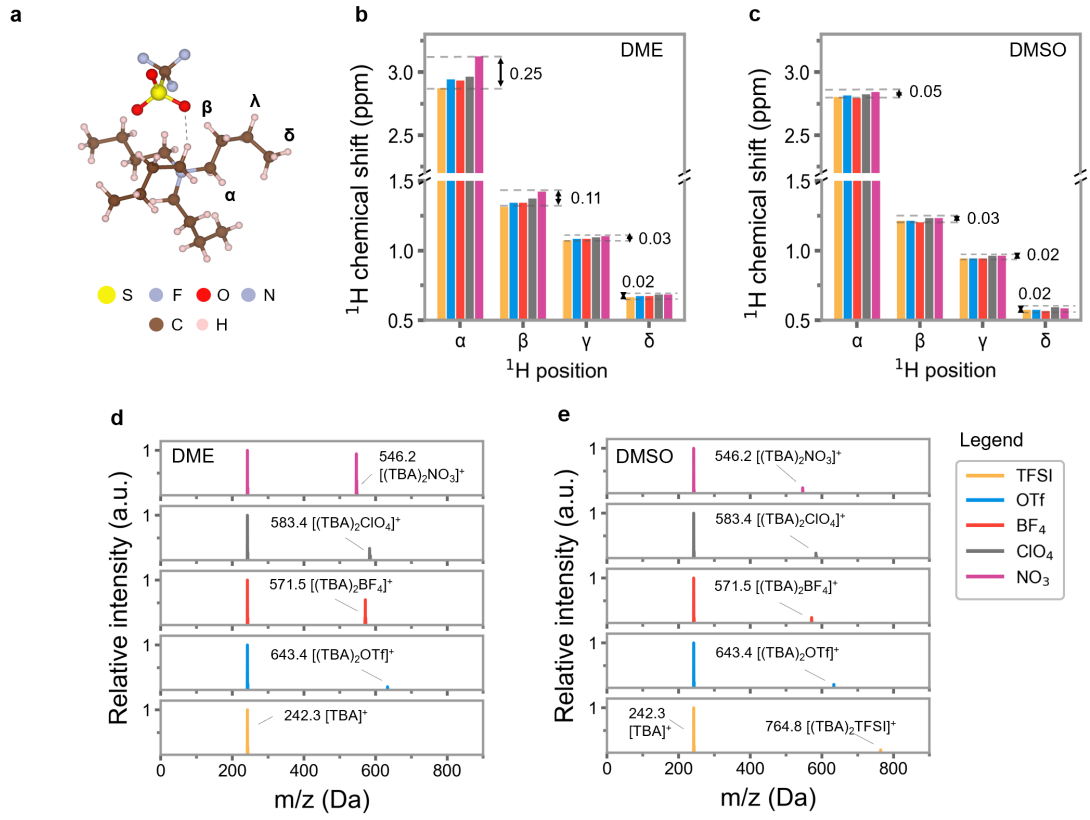

Figure 4. **Ion solvation**. (**a**) Illustration of TBA^+ cation interacting with an OTf^- anion and hydrogen labeling according to their relative position to the nitrogen atom in the TBA^+ structure. ^1H NMR chemical shift for 0.5M TBA^+ salts in (**b**) DME and (**c**) DMSO, and ESI-MS spectra (positive mode) for different TBA^+ salts (0.5M) in (**d**) DME and (**e**) DMSO. The abundance of the ion aggregates was normalized by the respective abundance of the free TBA^+ ions.

The influence of salt and solvent selection on the ionic solvation structure was probed using spectroscopic techniques. We first investigated the structures of all electrolytes in DME using ^1H-NMR (nuclear magnetic resonance) spectroscopy. Since the cation and solvent were kept constant across all salts, the differences in the ^1H chemical shifts from the TBA^+ can only then be attributed to differences in the interaction with the anion. Figure 4a. illustrates how a TBA^+ cation can interact with OTf^- anion through the more polarized hydrogens in the alpha position (α-H). Figures 4b and 4c show the ^1H chemical shifts for all protons present in the TBA^+ cation in the presence of different anions in DME and DMSO, respectively. As expected, the α-H protons were the most susceptible to ion-dipole interactions as the anion is changed. This preference can be observed by the greater differences in the chemical shift for the α-H among the anions in comparison to the protons in subsequent positions (β, λ, and δ) for both DME and DMSO.

As observed for other organic salts and ionic liquids, the chemical shift from the TBA^+ α-H can be correlated to the hydrogen bond acceptance ability of the anion. The smaller and planar structure of nitrate anions makes them a good hydrogen bond acceptor [64,65], resulting in a more downfield chemical shift for the α-H from the TBA when compared to other anions. On the other hand, salts containing weekly coordinating anions, such as BF_4^-, OTf^-, and $TFSI^-$ presented a more upfield chemical shift. Those differences in the chemical shift were more pronounced in the low dielectric constant DME than in DMSO, which presented a maximum α-H chemical shift gap across all TBA salts of 0.25 and 0.05 ppm, respectively. In general, the trends in α-H chemical shift in DME; $TFSI^- < BF_4^- < OTf^- < ClO_4^- < NO_3^-$ followed an inverse relation with the CO_2RR current density. As an exception, the solution containing BF_4^- anions had a more downfield α-H chemical shift when compared to OTf^- and ClO_4^- solutions, while presenting smaller current density values than those anions. We also observed that all TBA salts in DMSO presented similar and more upfield chemical shifts than in DME, while also presenting similar and higher values for current density.

We further investigated the TBA^+ solvation structures in DME and DMSO using electrospray ionization mass spectrometry (ESI-MS). By quantifying the relative abundance of all TBA^+ containing species, it is possible to map out the different ionic pairs within the TBA^+ solvation sheath. In general, ion pairs in the solution can be categorized in (i) contact ion pairs/aggregates,

which involves the direct contact of two/multiple ionic species with opposite charge in solution; and (ii) solvent-separated ion pairs, wherein the charged species are separated by one/multiple solvent molecules (see illustration of different solvation structures in Figure S4). In the ESI-MS spectra illustrated in Figures 4d and 4e, we did not observe any solvent-separated ion pairs for all TBA salts for both DME and DMSO respectively. These results indicate that the TBA^+ does not interact strongly with the solvent, even with the highly coordinating DMSO. However, the population of ion aggregates (composed of two TBA^+ and one anion) was a function of both solvent and anionic species.

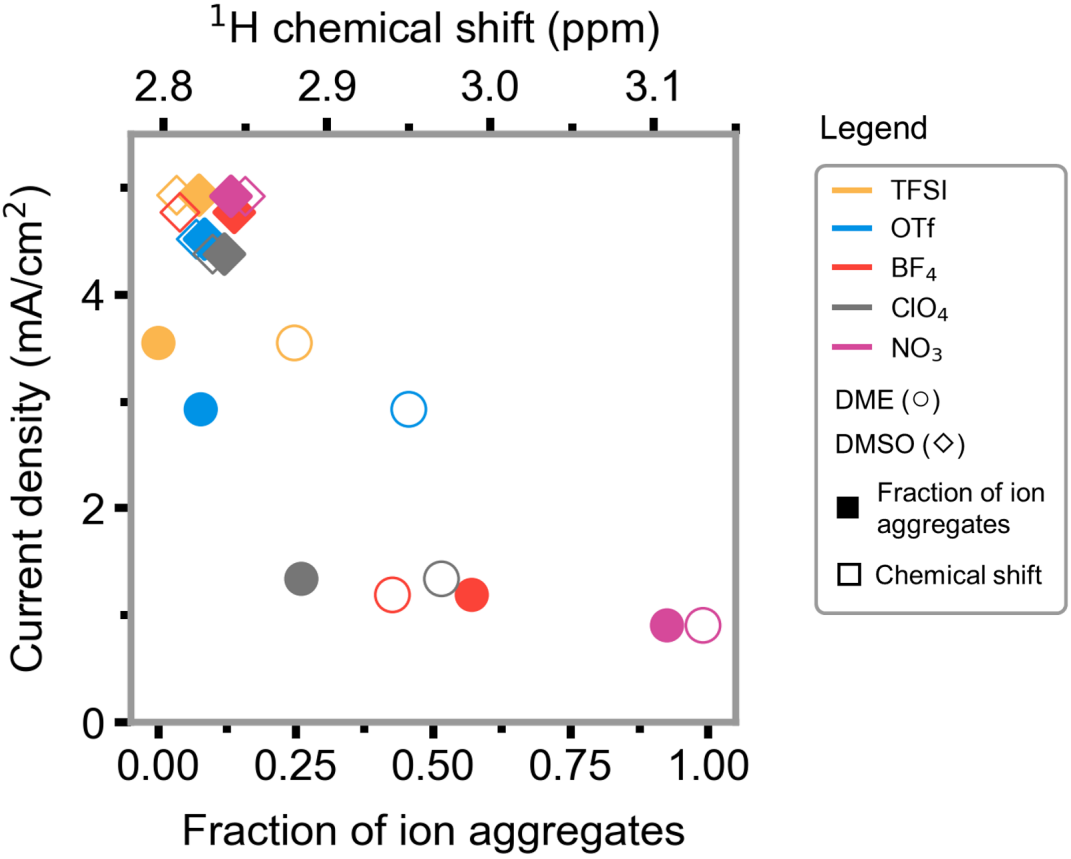

Figure 5. Solvation and electrochemistry correlation. Correlation between the current density extracted from the LSVs plots (Figures 3a and 3c) at -2.8V vs Fc* for Cu electrodes for different TBA salts in DME (circles) and DMSO (diamonds) *vs* (i) α-H chemical shifts from the TBA^+ (hollow icons) extracted from ^{1}H NMR results (Figures 4b and 4c) and (ii) fraction of ion aggregates (solid icons) extracted from ESI-MS results (Figures 4d and 4e).

The formation of ion aggregates can be attributed to the properties of both solvent and supporting electrolyte. On one hand, the solvent dielectric constant can be directly related to its ability to dissociate ions in solution[36,65]; which may explain the lower population of ion aggregates observed

for TBA^+ salts in DMSO (Figure 4e). On the other hand, the alkyl groups in the TBA^+ structure hinders its interactions with larger anions, such as OTf^- and $TFSI^-$. This anion effect on the population of ion aggregates was observed in DME, where the ions are not easily dissociated due to the medium low dielectric constant (Figure 4d). Our spectroscopic observations in Figure 4 can now be directly related to the electrochemical measurements. As depicted in Figure 5, while the fraction of ion aggregates increases in DME (moving from $TFSI^-/OTf^-$ to ClO_4^-, BF_4^-, and NO_3^-), the current density decreases. On the other hand, all TBA^+ salts presented a low population of ion aggregates and large CO_2RR current density values when dissolved in DMSO. We also observed a similar trend for the TBA^+ α-H chemical shift, where a more upfield chemical shift can be correlated to larger current density values not only across different salts in DME, but also across different solvents. We also probed the effect of solvent dielectric constant on the salt dissociation and electrochemical properties by using density functional theory (DFT) calculations[66], which show more negative complexation energy for all TBA salts in DME when compared to DMSO (Figure S5). Our observations are vital as we directly correlate bulk solvation behavior (as observed in NMR and ESI-MS) to electrochemical CO_2RR that occurs at the catalyst-electrolyte interface.

Electrolyte effect on product distribution

The effect of different TBA electrolytes on the CO_2RR product distribution was investigated using an asymmetric H-Cell setup (Figure S6). The different TBA solutions in DME were used as a catholyte, while the anolyte chamber was filled with a 0.5 M $TBAClO_4$ DME solution containing 0.5M water. The catholyte and anolyte chambers were separated by a Nafion® N-117 proton exchange membrane (PEM). When water is not added to the anolyte solution, either solvent or electrolyte oxidation takes place, leading to the appearance of a dark brown solution whose products could then react with the proton exchange membrane [7]. The addition of water also results in oxygen evolution as the dominant anodic reaction, ensuring a constant flow of protons to the cathodic chamber. The CO_2RR products in the gas and liquid phases were quantified using GC (gas chromatography) and ^{1}H-NMR, respectively (further described in the Supporting Information).

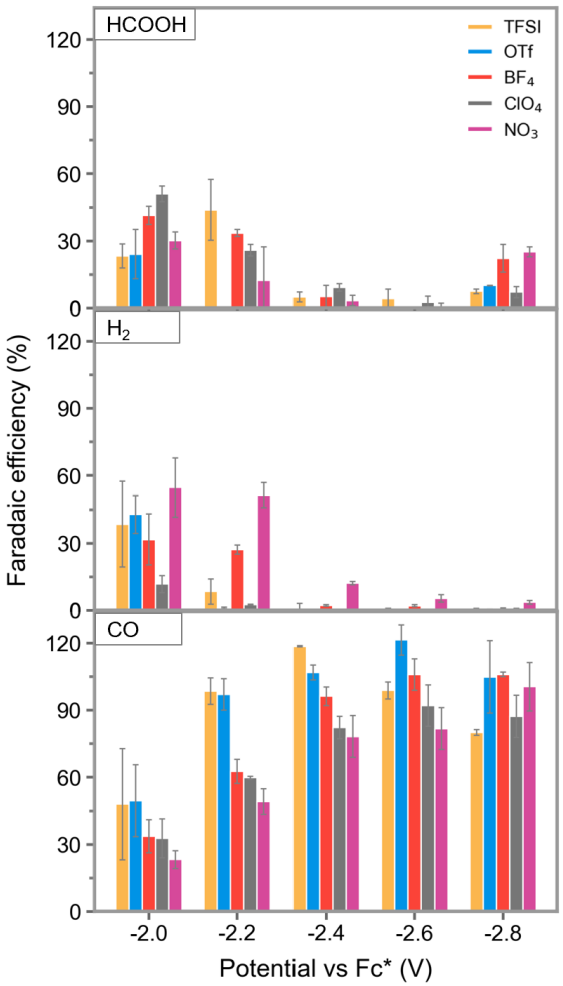

Figure 6. **Electrolyte effect on CO_2RR product distribution.** CO_2RR product distribution for different TBA salts (0.5M) in DME as catholyte and $TBAClO_4$ (0.5M) containing 0.5M of water in DME as an anolyte. A Cu disk (31.67 mm^2) was used as a cathode, a Ag/AgCl leakless electrode was used as a reference electrode, and Pt foil was used as an anode.

Figure 5 summarizes the effect of the electrolyte and the applied potential on the CO_2RR product distribution for Cu electrode. Herein, we only observed carbon monoxide, hydrogen, and formic acid as major CO_2RR products in DME. Our experiments conducted under an argon atmosphere (Figure S10) indicated that all products arise from CO_2RR rather than electrolyte/solvent decomposition. This product distribution is similar to what other authors have reported for Cu electrodes in nonaqueous electrolytes[14,30]. We also observed small amounts of methane at low overpotentials when TBAOTf was used as an electrolyte that can result from electrolyte decomposition (as seen with XPS data in Figure S3). We observed that both formic acid and methane production are electrode dependent since none of these two products were formed for a gold working electrode (Figure S11).

As a general trend, FE for CO increases with increasing overpotentials, reaching values above 90% at -2.6V for all electrolytes, and nearly 100% for OTf. The high FE values observed for CO for Cu electrode in DME are comparable with those found for noble metal electrodes such as Au and Ag in both aqueous and nonaqueous electrolytes[9,14,67]. Interestingly, at potentials below -2.6V, we found that OTf^- and $TFSI^-$ solutions presented similar or higher FE values for CO when compared to the remaining TBA salts. Hence it appears that the solvation effects we discussed earlier not only modulate current densities but also CO_2RR product distributions, especially at lower reductive potentials. This electrolyte effect in the CO_2RR selectivity can also be observed for experiments conducted in DMSO (Figure S12), where the low population of ion aggreagtes presented by both OTf^- and NO_3^- resulted in higher FE values for CO (at the same potentials) when compared to DME.

Even though all electrolyte solutions were prepared under dry conditions (below 100 ppm of water), the water content in the catholyte increased by one order of magnitude during CO_2RR (see Table S1). We hypothesize three sources for the water content increase: (i) Electrolytes can absorb moisture even from the inert Argon glovebox environment over the 12h experiment; (ii) Water can be generated *in situ*. The small amount of water could allow the CO_2RR to go through either a proton transfer or a proton-coupled electron transfer reaction[68]. Then, the generated OH^- could react with the protons that arise from the PEM, therefore forming more water; (iii) Water could also diffuse from the anolyte to the catholyte through the PEM[69]. Regardless of its source, water is most likely the main source of protons for the hydrogen gas observed in our product distribution analysis. Since HER is a competing reaction to CO_2RR, the FE values for hydrogen follow the opposite trend as for CO, reaching values close to zero as we moved to high overpotentials. Nevertheless, DME solutions containing NO_3^- ions with high ion pair formation presented significant amounts of hydrogen even at potentials as negative as -2.8V.

Conclusions

In conclusion, we investigated the effect of ion solvation on the CO_2 reduction reaction in aprotic solvents. Our voltammetric and XPS studies in DME showed that the presence of alkali cations can suppress CO_2RR by forming an insulating carbonate layer that prevents any further electrochemical reaction at the catalyst surface. In contrast, most tetrabutylammonium salts were able to sustain CO_2RR at potentials down to -2.8 V vs Fc* without any apparent decomposition. We also observed that the effect of the anion in the CO_2RR current density is strongly affected by the nature of the solvent. For the low coordinating DME solvent, $TFSI^-$ and OTf^- salts presented larger CO_2RR current density values when compared to BF_4^-, ClO_4^-, and NO_3^- salts. These results could not be ascribed only to differences either in solution conductivity, water content, or catalyst

surface modifications. In contrast, the same TBA salts when dissolved in the highly coordinating DMSO presented all similar current density values. Importantly, our spectroscopic studies showed that CO_2RR current density values in aprotic solvents could be correlated to differences in the electrolyte solvation structure. ^{1}H-NMR experiments indicated that a more upfield chemical shift in the α-Hs from TBA results in larger CO_2RR current density values, while ESI-MS measurements mirrored the NMR results by showing that an increase in current density is inversely related to the population of ion-aggregates in solution. These correlations could be observed not only across different solvents but also across different anions in DME, where the solvent low dielectric constant prevents complete dissociation of the TBA salt, therefore enhancing the anion effect on the formation of ion pairs. Finally, we observed that a lower population of ion-aggregates can also be correlated to higher FE values for CO and lower FE values for H_2 at lower overpotentials. Our findings show the impact of solvation behavior, such as the population of ion aggregates, in dictating CO_2RR product distribution and current density in different aprotic solvents relevant for integrated CO_2 capture and conversion.

Experimental section

Materials. Sodium perchlorate (98%), barium hydroxide octahydrate (98%), dimethoxyethane (anhydrous, 99.5%, inhibitor-free), diglyme (anhydrous, 99.5%), tetraglyme (anhydrous, 99%), dimethyl sulfoxide (anhydrous, 99.9%), 4Å molecular sieves, decamethylferrocene (97%), and tetrabutylammonium bis-trifluoromethanesulfonimidate (99%), and tetrafluoroborate (99%) were purchased from Sigma-Aldrich. Nafion N-117 membrane (0.18mm thick, >0.9 meq/g exchange capacity), and tetrabutylammonium triflate (99%), perchlorate (99%), and nitrate (99%) were purchased from Alfa-Aesar. Deuterated acetonitrile (≥99.8 atom % D) and deuterated dimethyl sulfoxide (≥99.8 atom % D) were purchased from Cambridge Isotope Laboratories. All solvents used for preparing electrolyte solutions were dried by 4 Å molecular sieves overnight (and stored with molecular sieves) inside an argon-filled glovebox (VigorTech, O_2 and H_2O < 1 ppm). All salts used in electrochemical experiments were vacuum dried at 90 °C overnight in a heated glovebox antechamber before use and was not exposed to air at any time. Other chemicals were used as received. The copper electrode was assembled by fitting the copper Super-conductive cooper rods (31.65 mm^2, 99.99%) rods into a PTFE tube, both purchased from McMaster-Carr. Platinum foils (99.99%) were acquired from BeanTown chemical, while gold disk electrodes (7.07 mm^2) and leakless miniature Ag/AgCl electrodes were purchased from eDAQ. Carbon dioxide gas (99.9995%) and argon gas (99.999%) were purchased from Airgas.

Electrochemical experiments. The voltammetric experiments were performed using a three-electrode configuration in a beaker cell (Figure S8a) at room temperature inside an argon-filled glovebox. A platinum foil was used as a counter electrode and a leakless miniature Ag/AgCl as a reference electrode. Before each experiment, the working electrodes (Cu and Au) were soaked in a 0.1M aqueous phosphoric acid solution for 1h, then polished with alumina suspension, rinsed with Milli-Q water (18.4 MΩ.cm), and sonicated for 10 min. The electrochemical potential was controlled using a Biologic VSP-300 Potentiostat and compensated for 85% of the value of R_u. The electrolyte solutions were purged with argon and CO_2 for 5 min for an experiment under argon and CO_2 atmosphere respectively. The value of the decamethylferrocene redox potential was first accessed using cyclic voltammetry measurements in a separated electrolyte solution containing 2mM Fc* to convert the Ag/Ag^+ to the Fc* scale. Since we observed that

DMSO decomposes at more positive potentials for a copper electrode, conversions to the Fc* scale were made using a gold electrode for the same electrolyte.

NMR spectroscopy for solvation studies. All NMR samples were prepared inside an Argon-filled glovebox using a coaxial capillary setup, where the electrolyte is placed inside a capillary tube (New Era Enterprises) and sealed with a PTFE cap from the surrounding deuterated solvent (D-acetonitrile)[48,70]. The deuterated solvent was contained inside an NMR tube (Wilmad), which was then capped and sealed with parafilm before analysis on a Bruker Ascend 9.4 T/400 MHz instrument. The ^{1}H chemical shift values were referenced to the residual non-deuterated acetonitrile (1.93 ppm). Since NMR signal for DME solvent hindered the signal from hydrogens in the alpha position (α-H) in the TBA cation, the chemical shifts for α-1H were determined using a 2D homonuclear correlation spectroscopy (COSY) experiment (Figure S5)

ESI-MS studies. All samples were prepared inside of the argon-filled glovebox and stored in 2 ml autosampler vials (ThermoFisher Scientific) to avoid major exposure to oxygen, which can accelerate glyme-ethers decomposition[47,71]. The samples were analyzed using an Agilent Technologies 1260 Infinity chromatograph equipped with an electrospray, quadrupole mass spectrometer detector (Agilent Technologies 6120; MSD). The fragmenting voltage in the MSD was 70 V and data were collected in the m/e range of 50 to 1000. Typically, 2-5 μL were directly injected into the MSD using a Hamilton syringe by hand. The mass spectral data were collected as full gaussians. The mass spectral data were analyzed with the methods of Malinowski[72]. Here, single-ion chromatograms were used to calculate the mass spectra as described in other works[73,74].

XPS Characterization. Copper foils were cut into strips (1 x 4 cm) and used as a working electrode in a three-electrode setup with Ag/AgCl as a reference electrode and platinum foil as a counter electrode. The electrolysis was performed inside an argon-filled glove box. The copper foils were not stored inside the glovebox to avoid contamination and they were used as received. After electrolysis, all the copper foils were rinsed three times with DME and dried for 1h at room temperature outside of the glove box. XPS experiments illustrated in Figure 1b and Figure S3 were performed on a Kratos Axis Nova spectrometer. Experiments in Figure 1c and 1d were performed using a PHI 5000 VersaProbe II System (Physical Electronics). The spectra were obtained using an Al Ka radiation (hν = 1486.6 eV) beam (100 μm, 25 W), Ar^{+} and electron beam sample neutralization, in Fixed Analyzer Transmission mode. XPS spectra were aligned to the

C-C component in the C1s spectra at 284.8 eV. Peak fitting was performed using Shirley background correction and the Gaussian–Lorentzian curve synthesis available in CasaXPS software[75].

Product distribution analysis. The CO_2RR product distribution was investigated using an H-cell setup (Figure S8b) inside the argon-filled glove box, where the platinum foil was used as a counter electrode, a leakless Ag/AgCl as a reference electrode, and copper rod as a working electrode. The catholyte compartment was filled with the electrolyte sample, while a solution containing 0.5M TBAClO4 and 0.5M water in the solvent of interest was used as an anolyte. Both chambers were separated by a Nafion-N117 proton exchange membrane. The catholyte was stirred at 1000 rpm while a constant CO_2 flow of 10 sccm was fed into the solution. The CO_2 inlet tubing was placed in a way that the gas bubble bubbles did not hit the cathode surface. Products in the gas phase were analyzed using a Shimadzu GC-2014 gas chromatograph with both flame ionization detector (FID) and thermal conductive detector (TCD). Products in the liquid phase were quantified using ^{1}H-NMR in a Bruker Ascend 9.4 T/400 MHz instrument. The methods and equations used for the calculation of the product distribution are further described in the supporting information.

Acknowledgments

This work was supported by generous start-up funds from the University of Chicago, the Neubauer Family Assistant Professors program, and by the University of Chicago Data Science Institute AI+Science seed funding. C.B. was supported by the UChicago Metcalf fellowship. NMR measurements were taken at the UChicago Chemistry NMR Facility and XPS measurements were partly done at the UChicago Chemistry XPS Facility and Argonne National Laboratory. The authors thank Alexander Filatov for performing part of the XPS experiments presented in this work.

References

1. Chen, A. & Lin, B.-L. A Simple Framework for Quantifying Electrochemical CO2 Fixation. *Joule* **2**, 594–606 (2018).

2. Phil, D. L. *et al.* What would it take for renewably powered electrosynthesis to displace petrochemical processes? *Science* **364**, eaav3506 (2019).

3. Shin, H., Hansen, K. U. & Jiao, F. Techno-economic assessment of low-temperature carbon dioxide electrolysis. *Nature Sustainability* **4**, 911–919 (2021).

4. Somoza-Tornos, A., Guerra, O. J., Crow, A. M., Smith, W. A. & Hodge, B.-M. Process modeling, techno-economic assessment, and life cycle assessment of the electrochemical reduction of CO2: a review. *Iscience* 102813 (2021).

5. Birdja, Y. Y. *et al.* Advances and challenges in understanding the electrocatalytic conversion of carbon dioxide to fuels. *Nature Energy* **4**, 732–745 (2019).

6. Bagger, A., Ju, W., Varela, A. S., Strasser, P. & Rossmeisl, J. Electrochemical CO2 Reduction: A Classification Problem. *ChemPhysChem* **18**, 3266–3273 (2017).

7. Ting, L. R. L. *et al.* Electrochemical Reduction of Carbon Dioxide to 1-Butanol on Oxide-Derived Copper. *Angewandte Chemie International Edition* **59**, 21072–21079 (2020).

8. Ooka, H., Figueiredo, M. C. & Koper, M. T. M. Competition between Hydrogen Evolution and Carbon Dioxide Reduction on Copper Electrodes in Mildly Acidic Media. *Langmuir* **33**, 9307–9313 (2017).

9. Goyal, A., Marcandalli, G., Mints, V. A. & Koper, M. T. M. Competition between CO2 Reduction and Hydrogen Evolution on a Gold Electrode under Well-Defined Mass Transport Conditions. *Journal of the American Chemical Society* **142**, 4154–4161 (2020).

10. Dinh, C.-T. *et al.* CO₂ electroreduction to ethylene via hydroxide-mediated copper catalysis at an abrupt interface. *Science* **360**, 783 LP – 787 (2018).

11. Rabinowitz, J. A. & Kanan, M. W. The future of low-temperature carbon dioxide electrolysis depends on solving one basic problem. *Nature Communications* **11**, 5231 (2020).

12. Amanchukwu, C. v. The Electrolyte Frontier: A Manifesto. *Joule* **4**, 281–285 (2020).

13. Medina-Ramos, J., DiMeglio, J. L. & Rosenthal, J. Efficient Reduction of CO2 to CO with High Current Density Using in Situ or ex Situ Prepared Bi-Based Materials. *Journal of the American Chemical Society* **136**, 8361–8367 (2014).

14. Ikeda, S., Takagi, T. & Ito, K. Selective Formation of Formic Acid, Oxalic Acid, and Carbon Monoxide by Electrochemical Reduction of Carbon Dioxide. *Bulletin of the Chemical Society of Japan* **60**, 2517–2522 (1987).

15. Tomita, Y. & Hori, Y. Electrochemical reduction of carbon dioxide at a platinum electrode in acetonitrile-water mixtures. in *Advances in Chemical Conversions for*

Mitigating Carbon Dioxide (eds. Inui, T., Anpo, M., Izui, K., Yanagida, S. & Yamaguchi, T. B. T.-S. in S. S. and C.) vol. 114 581–584 (Elsevier, 1998).

16. Zhu, Q. *et al.* Efficient Reduction of CO2 into Formic Acid on a Lead or Tin Electrode using an Ionic Liquid Catholyte Mixture. *Angewandte Chemie International Edition* **55**, 9012–9016 (2016).

17. Fischer, J., Lehmann, T. & Heitz, E. The production of oxalic acid from CO 2 and H 2 O. *Journal of Applied Electrochemistry* **11**, 743–750 (1981).

18. König, M., Vaes, J., Klemm, E. & Pant, D. Solvents and Supporting Electrolytes in the Electrocatalytic Reduction of CO2. *iScience* (2019) doi:10.1016/j.isci.2019.07.014.

19. Gennaro, A., Isse, A. A. & Vianello, E. Solubility and electrochemical determination of CO2 in some dipolar aprotic solvents. *Journal of Electroanalytical Chemistry* (1990) doi:10.1016/0022-0728(90)87217-8.

20. Bucklin, R. W. & Schendel, R. L. Comparison of fluor solvent and selexol processes. *Energy Prog.;(United States)* **4**, (1984).

21. Burr, B. & Lyddon, L. A comparison of physical solvents for acid gas removal, Bryan Research & Engineering. *Inc., Bryan, Texas, USA* (2008).

22. Li, J. *et al.* Hydroxide Is Not a Promoter of C2+ Product Formation in the Electrochemical Reduction of CO on Copper. *Angewandte Chemie International Edition* **59**, 4464–4469 (2020).

23. Hori, Y., Kikuchi, K., Murata, A. & Suzuki, S. PRODUCTION OF METHANE AND ETHYLENE IN ELECTROCHEMICAL REDUCTION OF CARBON DIOXIDE AT COPPER ELECTRODE IN AQUEOUS HYDROGENCARBONATE SOLUTION. *Chemistry Letters* **15**, 897–898 (1986).

24. Hatsukade, T., Kuhl, K. P., Cave, E. R., Abram, D. N. & Jaramillo, T. F. Insights into the electrocatalytic reduction of CO2 on metallic silver surfaces. *Physical Chemistry Chemical Physics* **16**, 13814–13819 (2014).

25. Gao, D., Scholten, F. & Roldan Cuenya, B. Improved CO2 Electroreduction Performance on Plasma-Activated Cu Catalysts via Electrolyte Design: Halide Effect. *ACS Catalysis* **7**, 5112–5120 (2017).

26. Varela, A. S., Kroschel, M., Reier, T. & Strasser, P. Controlling the selectivity of CO2 electroreduction on copper: The effect of the electrolyte concentration and the importance of the local pH. *Catalysis Today* (2016) doi:10.1016/j.cattod.2015.06.009.

27. Huang, Y., Ong, C. W. & Yeo, B. S. Effects of Electrolyte Anions on the Reduction of Carbon Dioxide to Ethylene and Ethanol on Copper (100) and (111) Surfaces. *ChemSusChem* **11**, 3299–3306 (2018).

28. Berto, T. C., Zhang, L., Hamers, R. J. & Berry, J. F. Electrolyte Dependence of CO2 Electroreduction: Tetraalkylammonium Ions Are Not Electrocatalysts. *ACS Catalysis* **5**, 703–707 (2015).

29. Niu, D., Wang, H., Li, H. & Zhang, X. The effect of the alkyl chain length of the tetraalkylammonium cation on CO2 electroreduction in an aprotic medium. *Electrochemistry Communications* **52**, 58–62 (2015).

30. Figueiredo, M. C., Ledezma-Yanez, I. & Koper, M. T. M. In Situ Spectroscopic Study of CO2 Electroreduction at Copper Electrodes in Acetonitrile. *ACS Catalysis* **6**, 2382–2392 (2016).

31. Amanchukwu, C. v, Chang, H.-H. & Hammond, P. T. Influence of Ammonium Salts on Discharge and Charge of Li–O2 Batteries. *The Journal of Physical Chemistry C* **121**, 17671–17681 (2017).

32. Amanchukwu, C. v *et al.* One-Electron Mechanism in a Gel–Polymer Electrolyte Li–O2 Battery. *Chemistry of Materials* **28**, 7167–7177 (2016).

33. Lutz, L. *et al.* Role of Electrolyte Anions in the Na–O2 Battery: Implications for NaO2 Solvation and the Stability of the Sodium Solid Electrolyte Interphase in Glyme Ethers. *Chemistry of Materials* **29**, 6066–6075 (2017).

34. Johnson, L. *et al.* The role of LiO 2 solubility in O 2 reduction in aprotic solvents and its consequences for Li–O 2 batteries. *Nature chemistry* **6**, 1091–1099 (2014).

35. Lutz, L. *et al.* High Capacity Na–O2 Batteries: Key Parameters for Solution-Mediated Discharge. *The Journal of Physical Chemistry C* **120**, 20068–20076 (2016).

36. Giesecke, M. *et al.* Ion association in aqueous and non-aqueous solutions probed by diffusion and electrophoretic NMR. *Physical Chemistry Chemical Physics* **17**, 3402–3408 (2015).

37. Sharon, D. *et al.* Mechanistic Role of Li+ Dissociation Level in Aprotic Li–O2 Battery. *ACS Applied Materials & Interfaces* **8**, 5300–5307 (2016).

38. Choi, N.-S. *et al.* Challenges Facing Lithium Batteries and Electrical Double-Layer Capacitors. *Angewandte Chemie International Edition* **51**, 9994–10024 (2012).

39. Hobold, G. M. *et al.* Moving beyond 99.9% Coulombic efficiency for lithium anodes in liquid electrolytes. *Nature Energy* **6**, 951–960 (2021).

40. Jache, B., Binder, J. O., Abe, T. & Adelhelm, P. A comparative study on the impact of different glymes and their derivatives as electrolyte solvents for graphite co-intercalation electrodes in lithium-ion and sodium-ion batteries. *Physical Chemistry Chemical Physics* **18**, 14299–14316 (2016).

41. Ruther, R. E. *et al.* Mechanically Robust, Sodium-Ion Conducting Membranes for Nonaqueous Redox Flow Batteries. *ACS Energy Letters* **3**, 1640–1647 (2018).

42. Banerjee, S., Han, X. & Thoi, V. S. Modulating the Electrode–Electrolyte Interface with Cationic Surfactants in Carbon Dioxide Reduction. *ACS Catalysis* **9**, 5631–5637 (2019).

43. Kuhl, K. P., Cave, E. R., Abram, D. N. & Jaramillo, T. F. New insights into the electrochemical reduction of carbon dioxide on metallic copper surfaces. *Energy & Environmental Science* **5**, 7050–7059 (2012).

44. Noviandri, I. *et al.* The Decamethylferrocenium/Decamethylferrocene Redox Couple: A Superior Redox Standard to the Ferrocenium/Ferrocene Redox Couple for Studying Solvent Effects on the Thermodynamics of Electron Transfer. *The Journal of Physical Chemistry B* **103**, 6713–6722 (1999).

45. Kwabi, D. G. *et al.* Experimental and Computational Analysis of the Solvent-Dependent O2/Li+-O2− Redox Couple: Standard Potentials, Coupling Strength, and Implications

for Lithium–Oxygen Batteries. *Angewandte Chemie International Edition* **55**, 3129–3134 (2016).

46. Setterfield-Price, B. M. & Dryfe, R. A. W. The influence of electrolyte identity upon the electro-reduction of CO2 . *Journal of Electroanalytical Chemistry* **730**, 48–58 (2014).

47. Freunberger, S. A. *et al.* The Lithium–Oxygen Battery with Ether-Based Electrolytes. *Angewandte Chemie International Edition* **50**, 8609–8613 (2011).

48. Ma, P., Mirmira, P. & Amanchukwu, C. v. Effect of Building Block Connectivity and Ion Solvation on Electrochemical Stability and Ionic Conductivity in Novel Fluoroether Electrolytes. *ACS Central Science* **7**, 1232–1244 (2021).

49. Xie, Z., Zhang, X., Zhang, Z. & Zhou, Z. Metal–CO2 Batteries on the Road: CO2 from Contamination Gas to Energy Source. *Advanced Materials* **29**, 1605891 (2017).

50. Xu, S., Lau, S. & Archer, L. A. CO2 and ambient air in metal–oxygen batteries: steps towards reality. *Inorganic Chemistry Frontiers* **2**, 1070–1079 (2015).

51. Zhang, X., Yang, H. & Bard, A. J. Variation of the heterogeneous electron-transfer rate constant with solution viscosity: reduction of aqueous solutions of [(EDTA)chromium(III)]- at a mercury electrode. *Journal of the American Chemical Society* **109**, 1916–1920 (1987).

52. Riadigos, C. F., Iglesias, R., Rivas, M. A. & Iglesias, T. P. Permittivity and density of the systems (monoglyme, diglyme, triglyme, or tetraglyme+n-heptane) at several temperatures. *The Journal of Chemical Thermodynamics* **43**, 275–283 (2011).

53. Jache, B., Binder, J. O., Abe, T. & Adelhelm, P. A comparative study on the impact of different glymes and their derivatives as electrolyte solvents for graphite co-intercalation electrodes in lithium-ion and sodium-ion batteries. *Physical Chemistry Chemical Physics* **18**, 14299–14316 (2016).

54. Schmid, R. Re-interpretation of the solvent dielectric constant in coordination chemical terms. *Journal of Solution Chemistry* **12**, 135–152 (1983).

55. Black, J. J., Dolan, A., Harper, J. B. & Aldous, L. Kamlet–Taft solvent parameters, NMR spectroscopic analysis and thermoelectrochemistry of lithium–glyme solvate ionic liquids and their dilute solutions. *Physical Chemistry Chemical Physics* **20**, 16558–16567 (2018).

56. Welford, P. J. *et al.* The Electro-reduction of Carbon Dioxide in Dimethyl Sulfoxide at Gold Microdisk Electrodes: Current | Voltage Waveshape Analysis. *The Journal of Physical Chemistry B* **105**, 5253–5261 (2001).

57. LeBel, R. G. & Goring, D. A. I. Density, Viscosity, Refractive Index, and Hygroscopicity of Mixtures of Water and Dimethyl Sulfoxide. *Journal of Chemical & Engineering Data* **7**, 100–101 (1962).

58. Gennaro, A. *et al.* Mechanism of the electrochemical reduction of carbon dioxide at inert electrodes in media of low proton availability. *Journal of the Chemical Society, Faraday Transactions* **92**, 3963–3968 (1996).

59. Matsubara, Y., Grills, D. C. & Kuwahara, Y. Thermodynamic Aspects of Electrocatalytic CO2 Reduction in Acetonitrile and with an Ionic Liquid as Solvent or Electrolyte. *ACS Catalysis* **5**, 6440–6452 (2015).

60. Ringe, S. *et al.* Understanding cation effects in electrochemical CO2 reduction. *Energy & Environmental Science* **12**, 3001–3014 (2019).

61. Resasco, J. *et al.* Promoter Effects of Alkali Metal Cations on the Electrochemical Reduction of Carbon Dioxide. *Journal of the American Chemical Society* **139**, 11277–11287 (2017).

62. Monteiro, M. C. O. *et al.* Absence of CO2 electroreduction on copper, gold and silver electrodes without metal cations in solution. *Nature Catalysis* (2021) doi:10.1038/s41929-021-00655-5.

63. Shi, J. *et al.* Electrochemical reduction of CO2 into CO in tetrabutylammonium perchlorate/propylene carbonate: Water effects and mechanism. *Electrochimica Acta* **240**, 114–121 (2017).

64. Huynh, H. V., Lam, T. T. & Luong, H. T. T. Anion influences on reactivity and NMR spectroscopic features of NHC precursors. *RSC Advances* **8**, 34960–34966 (2018).

65. Pike, S. J., Hutchinson, J. J. & Hunter, C. A. H-Bond Acceptor Parameters for Anions. *Journal of the American Chemical Society* **139**, 6700–6706 (2017).

66. Kohn, W. & Sham, L. J. Self-Consistent Equations Including Exchange and Correlation Effects. *Physical Review* **140**, A1133–A1138 (1965).

67. Lu, Q. *et al.* A selective and efficient electrocatalyst for carbon dioxide reduction. *Nature Communications* **5**, 3242 (2014).

68. Dunwell, M., Luc, W., Yan, Y., Jiao, F. & Xu, B. Understanding Surface-Mediated Electrochemical Reactions: CO2 Reduction and Beyond. *ACS Catalysis* **8**, 8121–8129 (2018).

69. Thieu, L. M., Zhu, L., Korovich, A. G., Hickner, M. A. & Madsen, L. A. Multiscale Tortuous Diffusion in Anion and Cation Exchange Membranes. *Macromolecules* **52**, 24–35 (2019).

70. Amanchukwu, C. v, Kong, X., Qin, J., Cui, Y. & Bao, Z. Nonpolar Alkanes Modify Lithium-Ion Solvation for Improved Lithium Deposition and Stripping. *Advanced Energy Materials* **9**, 1902116 (2019).

71. Black, R. *et al.* The Nature and Impact of Side Reactions in Glyme-based Sodium–Oxygen Batteries. *ChemSusChem* **9**, 1795–1803 (2016).

72. Factor analysis in chemistry, (3rd edition). E. R. Malinowski, Wiley, New York, 2002, ISBN 0-471-13479-1, € 117.60. *Journal of Chemometrics* **16**, 635 (2002).

73. Dietz Rago, N. *et al.* Effect of overcharge on Li(Ni0.5Mn0.3Co0.2)O2/Graphite lithium ion cells with poly(vinylidene fluoride) binder. I - Microstructural changes in the anode. *Journal of Power Sources* **385**, 148–155 (2018).

74. Bloom, I. *et al.* Effect of overcharge on Li(Ni0.5Mn0.3Co0.2)O2 cathodes: NMP-soluble binder. II — Chemical changes in the anode. *Journal of Power Sources* **385**, 156–164 (2018).

75. Fairley, N. *et al.* Systematic and collaborative approach to problem solving using X-ray photoelectron spectroscopy. *Applied Surface Science Advances* **5**, 100112 (2021).